

# Design of a Compact Hard X-ray Split-Delay System Based on Variable-Gap Channelcut Crystals

Yanwen Sun<sup>1,2</sup>, Aymeric Robert<sup>1</sup> and Diling Zhu<sup>1,a)</sup>

<sup>1</sup>*Linac Coherent Light Source, SLAC National Accelerator Laboratory, Sand Hill Rd., Menlo Park, California, 94025, U.S.A.*

<sup>2</sup>*Physics Department, Stanford University, 382 Via Pueblo Mall, Stanford, California, 94305, U.S.A.*

<sup>a)</sup>Corresponding author: dlzhu@slac.stanford.edu

**Abstract.** Free Electron Lasers provide unique opportunities in investigating ultrafast atomic-scale dynamics using X-ray Pump X-ray Probe and two-pulse X-ray Speckle Visibility Spectroscopy techniques. However the performance of these techniques critically relies on maintaining the spatial overlap between the two beams at the sample location while adjusting the temporal separation between the two pulses. This presents major challenges for realizing hard X-ray split-delay optics, i.e an optical arrangement capable of generating two X-ray pulses separated in time from a single X-ray pulse. More specifically, it translates into nanoradian-scale angular precision requirements. We present here a hard X-ray split-delay optics concept using 4 channelcut crystals, where the beam path length difference can be adjusted by the linear translation of two crystals having non-parallel gaps. Having two Bragg reflections from the same monolithic crystal in the opposite direction cancels positioning errors from underlying stages. As a result, this concept has lower motion precision requirements on the hardware, and yet leads to significantly higher output beam angular stability. We present a case study for this concept that covers an energy range from 7 to 12 keV and provides a delay range from -3 to 10 ps at 9 keV.

## INTRODUCTION

The successful commissioning and operation of X-ray Free Electron Laser (FEL) facilities across the globe have enabled many new X-ray experiment techniques with great scientific potentials [1, 2, 3, 4, 5, 6]. Many recent developments in new FEL operation modes provided more than one single X-ray pulse to be used for advanced experimental schemes such as X-ray Pump X-ray Probe (XPXP), X-ray Speckle Visibility Spectroscopy (XSVS), and the observation of nonlinear X-ray phenomena [7, 8, 9, 10, 11, 12]. Another promising approach to produce two X-ray pulses with femto- to pico-second temporal spacing relies on using split-delay X-ray optics. They consist of an optical arrangement capable of splitting and recombining x-ray beams, thus generating two X-ray pulses from a single X-ray pulse that are separated in time. In the hard X-ray regime, using crystal reflections, the pioneering experimental efforts by Roseker *et al.* [13] and Osaka *et al.* [14] have demonstrated the viability of these approaches. This was further confirmed by the commissioning of such a split-delay optics system at the LCLS [15]. The lessons learned from operating these complex optics systems however revealed that the relative stability between the two output beams still requires significant improvements.

For the split-delay optics design, the most demanding motion requirement is described by Osaka *et al.* as the straightness of the linear motion required for adjusting the delay time between the two pulses [14]. To illustrate this further, we consider here typical parameters of some of the LCLS hard X-ray instruments [16, 17] that are located about 200-400 m from the source. Any unintended angular motion of the crystals in the delayed branch, such as the parasitic angular error while adjusting the linear position required for changing the time delay, will result in a change of the parallelism between the two output beams. This translates into a relative position shift between the two foci at the sample position. For a focal spot size of  $\sim 2 \mu\text{m}$  typically provided by a 4 m focal length optical focusing arrangement, the typical maximum acceptable misalignment between the two beams is typically considered to be 10% of the beam size, i.e. 200 nm. The combined angular error of the two linear motions when changing the delay-time must thus be below 25 nrad. Such angular error requirement is 2 orders of magnitude smaller than typical angular

errors of commercially-available metrology grade linear translation stages [15]. Without the ability to fulfill the level of angular precision described above, such optics would be constrained to operate with larger beam sizes and limited time-range before re-alignment is needed.

In this paper, we present an alternative concept of a hard X-ray split-delay optical layout consisting of 4 channelcut crystals (CC), within which two of them have nonparallel gaps as shown in Fig. 1. The delay between the two branches is adjusted via symmetric linear horizontal translations of these CCs with nonparallel gaps. This concept significantly reduces the requirement on the precision of the motion for time delay adjustments, in particular, the pitch/yaw error of the linear stages. It should allow performing fast and continuous delay scans while maintaining sufficient spatial overlap. It would thus greatly enhance both XSVS and XPCS measurements requiring focal spot sizes much smaller than what is possible now, albeit with a smaller delay range.

## CONCEPT AND DESIGN CONSIDERATIONS

As shown in Fig. 1, the proposed compact split-delay concept consists of 4 channelcut crystals. For discussion throughout this letter, we consider Si(220) reflections in  $\pi$  polarization in consistence with the horizontal polarization of the current FEL facilities and a horizontal scattering plane. The fix-delay branch is composed of a pair of ‘standard’ channelcut crystals CC1 and CC2. In contrast, the delay-adjustable branch consists of two channel-cuts VCC1 and VCC2, where a miscut is introduced on one of the two surfaces for each crystal. The non-parallel surfaces thus allow the ‘effective’ gap to be adjusted depending on the incident beam position on the first crystal reflection surface. As the geometric gap is *varying* across these channel-cuts, we term this split-delay concept the Variable-gap Channel-Cut Split-Delay (VCCSD). The beam splitting and recombination are realized by polishing the upper edge of the shorter crystal faces on CC1 and CC2 as indicated in Fig. 1. Each incoming FEL pulse is split at the polished edge of CC1. The lower part of the beam (red) is routed to the fix-delay branch and the upper part part (blue) glances over to the delayed branch. The two split-pulses are then recombined spatially at the downstream polished edge of CC2.

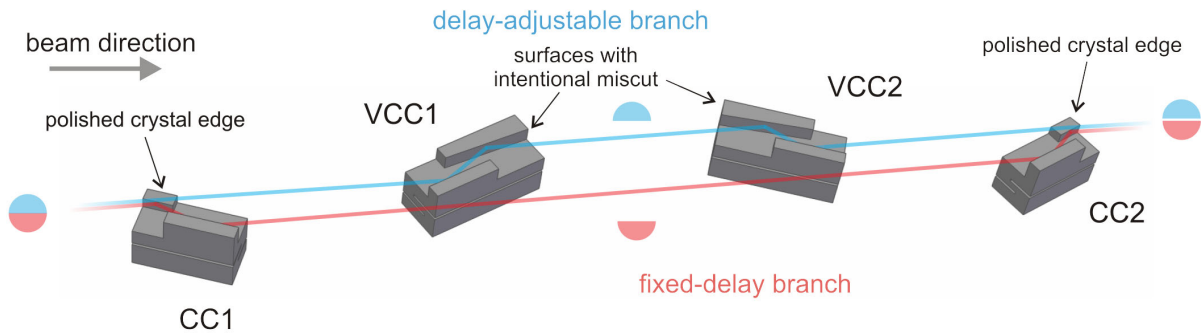


**FIGURE 1.** Schematic illustration of the Variable-gap Channel-Cut X-ray Split-Delay concept. The beam is split at the first edge reflection of CC1 and recombined at the second edge reflection of CC2. The pair of variable-gap channel-cuts VCC1 and VCC2 forms the delay adjustable branch.

The details of the dimensions of the Variable-gap Channel-Cut (VCC) considered in this study are provided in the inset of Fig. 2(b). The time delay between the two pulses can be calculated by the path length difference between the two branches. The delay range of this split-delay system is determined by the miscut angle  $\delta$ , the length of the VCC reflecting surfaces  $L$ , and the Bragg angle  $\theta_B$ , following the expression:

$$\text{delay time range} = \frac{2L \cdot (1 - \cos 2\theta_B) \cdot \sin \delta}{c \cdot \sin(\theta_B + \delta)}, \quad (1)$$

where  $c$  is the speed of light. For a working length of the non-asymmetric surface of VCC1 and VCC2 of  $L=40$  mm, the resulting expected delay range coverage is plotted in Fig. 2(a) as a function of the VCC surface miscut angle for photon energies from 7 to 12 keV.

The increased stability and tolerance against parasitic motion errors of this concept results from always having ‘paired’ reflections from a monolithic crystal. Since any angular motion errors apply to both reflections in opposite

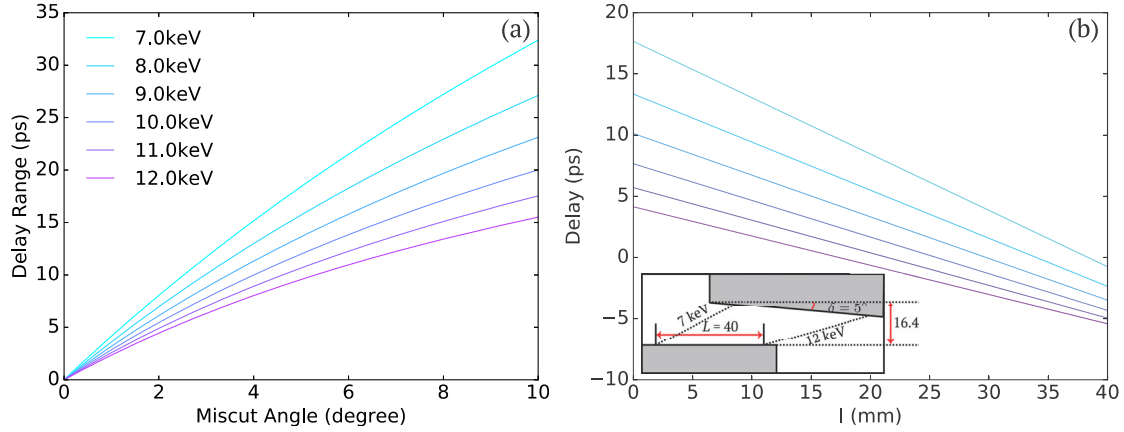


**FIGURE 2.** (a) Calculated time delay range as a function of the miscut angle  $\delta$  for several photon energies between 7 to 12 keV, assuming a  $L = 40$  mm long VCC surface. (b) X-ray photon energy dependence of the time delay coverage as a function of  $l$  with a miscut angle of  $\delta = 5^\circ$ . Here  $l$  is the distance between the reflection point of the beam and the outer reflecting edge on the symmetric reflection surface of the VCC. Units in the inset are in mm.

directions, they could cancel each other. As observed by Osaka *et. al* for the Split-Delay optics at SACLA [14], the channelcut branch shows significantly better stability as compared to that of the ‘upper’ branch consisting of 4 individual crystals. This advantage offered by monolithic crystals was also used successfully in various X-ray interferometer designs, as for example, a triple-Laue (LLL) crystal interferometer [18].

To fully understand the behavior of the two asymmetric reflections in the proposed setup, we need to consider the dynamical diffraction and the index-of-refraction effects [19, 20, 21]. Some of the expected behaviors include: (1) a change in the Darwin width, (2) a shift of rocking curve center as compared to the nominal Bragg angle, and (3) dispersion introduced by the asymmetric reflections. First, we need to identify a miscut angle such that the resulting shift in the rocking curve center is small as compared to the rocking curve width. While for a symmetric reflection, the incident and exit rocking curve center shifts are equal, this is not the case for asymmetric reflection. The asymmetry factor  $b$  is defined by:

$$b = \frac{\sin(\theta_B + \delta)}{\sin(\theta_B - \delta)}. \quad (2)$$

The incident/exit beam rocking curve center displacement  $\Delta\theta_c^i, \Delta\theta_c^e$  as compared to that of the symmetric reflection [21] are expressed as:

$$\Delta\theta_c^i = \frac{\sqrt{2}}{6} \frac{|F_{000}|}{|F_{hkl}|} \frac{(1-b)}{bP} \Delta\theta_d, \quad (3)$$

$$\Delta\theta_c^e = \frac{\sqrt{2}}{6} \frac{|F_{000}|}{|F_{hkl}|} \frac{(b-1)}{P} \Delta\theta_d, \quad (4)$$

where  $F_{hkl}$  is the structure factor for diffraction from crystal lattice plane with miller indices  $h,k,l$ , and  $P$  is the polarization factor. For  $\delta = 5^\circ$ , the shift in position of the rocking curves due to the index of refraction is below 40% of the width of the rocking curve. The resulting angular acceptance angle  $\Delta\theta_o$  for each of the channel-cuts is at least 5 times bigger than the incoming beam divergence for the energy range of the proposed system. Calculated values are listed in Table. 1 for X-ray photon energy of 9 keV.

With  $\delta = 5^\circ$  and  $L = 40$  mm, the dimensions of VCC1/2 can be determined and optimized, as shown in the inset of Fig. 2(b). The maximum gap size is set to be 16.4 mm to ensure the reflected X-ray beam can exit the channelcut crystal. The gap size for the fixed gap channelcut crystals (CC1, CC2) is set to be 12.7 mm in order to offer the possibility to access negative delay times at all X-ray photon energies. The time delay coverage is calculated with Eq. 1 and displayed in Fig. 2(b). The delay range varies from 18.4 ps at 7 keV down to 9.6 ps at 12 keV. Time-zero can be shifted within these ranges by choosing for CC1/2 slightly different gap sizes. As only four rotations are

**TABLE 1.** Widths and center shifts of the rocking curve at 9 keV assuming a  $\delta = 5^\circ$  miscut for both VCC1 and VCC2. Note that the two asymmetric reflections have opposite asymmetry factor.  $\Delta\theta_d$  is the Darwin width for the symmetric reflection case,  $\Delta\theta_a$  is the Darwin width for the asymmetric case, and  $\Delta\theta_c$  is the shift of the center of rocking curve with respect to the symmetric case.

	VCC1	VCC2
$b$	1.6	0.6
$\Delta\theta_d$	17.6 $\mu\text{rad}$	17.6 $\mu\text{rad}$
$\Delta\theta_a$	14.0 $\mu\text{rad}$	22.2 $\mu\text{rad}$
$\Delta\theta_c^i$	-3.3 $\mu\text{rad}$	5.2 $\mu\text{rad}$
$\Delta\theta_c^e$	5.2 $\mu\text{rad}$	-3.3 $\mu\text{rad}$
ang. accept. $\Delta\theta_o$	12.5 $\mu\text{rad}$	19.8 $\mu\text{rad}$

required in the present concept, i.e. one per channelcut crystal, the entire optical arrangement offers the possibility to be very compact as compared to existing or planned split-delays [13, 15, 22].

Note that one feature of the asymmetric reflection is that the exit beam from the CC is no longer parallel to the incoming beam as in the normal channelcut case. The angular difference varies while the incidence angle  $\theta_i$  slightly changes within the rocking curve. Unlike symmetric reflections where  $\Delta\theta_e = \Delta\theta_i$ , asymmetric geometries give  $\Delta\theta_e = b \cdot \Delta\theta_i$ . As a result, a small unintended in plane rotation of  $\partial\theta$  can still lead to a change in beam exit angle by  $(b - 1)\partial\theta$  [19, 20]. Compared to same the rotation of a single symmetric reflection that would lead to an exit beam angular change of  $2\partial\theta$ , the effect is reduced by a factor of  $(b - 1)/2$ . In directions out of the scattering plane, the reflection behaviors are specular, thus the angular errors in those directions fully cancel.

## DISCUSSION

The study described before only assumed a parallel and monochromatic beam. We further evaluate how the proposed concept performs in real experimental conditions by considering the non-zero spatial extent, the finite bandwidth, and the finite divergence, of the incoming X-ray beam. With realistic and typical LCLS parameters, a beam size on the order of 500  $\mu\text{m}$  should be considered; together with a pink beam bandwidth on the order of 20-30 eV. Typical LCLS monochromators use Si(111) or C\*(111) reflections, and therefore reduce the bandwidth from the pink beam to  $\sim 0.5$ -1.5 eV [17]. The impacts of these parameters on the performance of the proposed split-delay are discussed in more details in the following sections.

### Pulse Front Tilt And Pulse Stretching

The same mechanism that allows to adjust the relative delay also introduces a pulse front tilt across the X-ray beam in the diffraction plane, as illustrated in the inset of Fig. 3. Different parts of the beam effectively see slightly different CC gap. The 1D pulse front tilt of the exit beam from a single asymmetric reflection can be calculated following a similar formalism as the one used for the evaluation of the delay range. The pulse stretching  $\Delta\tau$  can be expressed as:

$$\frac{\Delta\tau}{\Delta x} = \frac{2 \sin \delta \cdot \sin \theta_B}{c \cdot \sin(\theta_B + \delta)}, \quad (5)$$

where  $\Delta x$  is the spatial dimension of the beam in the diffraction plane,  $c$  is the speed of light,  $\delta$  the miscut angle, and  $\theta_B$  the Bragg angle. Fig. 3 presents the calculated temporal spread  $\Delta\tau$  of the beam downstream of the split-delay for beam spot sizes of  $\Delta x = 500 \mu\text{m}$ . The temporal spread is significant (i.e.  $\approx 0.45$  ps) with a miscut angle  $\delta = 5^\circ$  as

compared to typical LCLS pulse duration of 20-30 fs. It can be reduced by using slits before the split-delay to limit the beam size, or by reducing the crystal miscut angle.

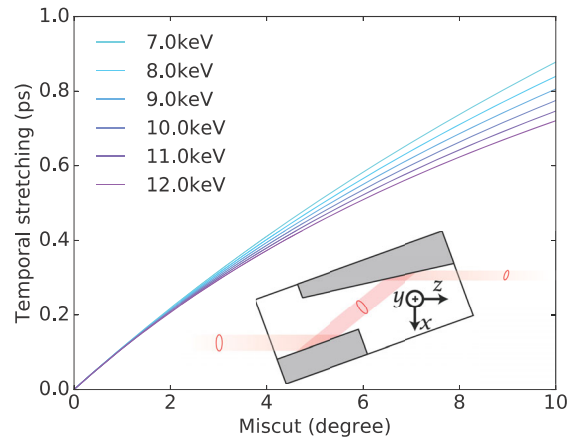


**FIGURE 3.** Temporal stretching from a pair of reflections through VCC assuming a  $\Delta x = 500 \mu\text{m}$  beamsize as a function of the miscut angle  $\delta$ . The inset is an illustration of the pulse front tilt due to the asymmetric reflection.

While the effective pulse lengthening effect reduces the time resolution of the split-delay, the tilted pulse front can on the other hand be utilized for X-ray streaking type applications [23, 24]. One example using the tilted pulse front is the single-shot measurement of the coherence length of a seeded FEL pulse. For example, at 8.3 keV, the self-seeded FEL pulse has a narrower bandwidth than Si(220) [25]. The recombined beams are vertically separated and can be superimposed by using an X-ray prism to deflect the beam from the fix-delay branch, and the two overlapped beams will form interference fringes at time delay zero. Due to the horizontal beam streaking, for each single shot, the longitudinal coherence can be extracted from the width of the region with high interference fringe visibility.

### Effect of Finite Bandwidth

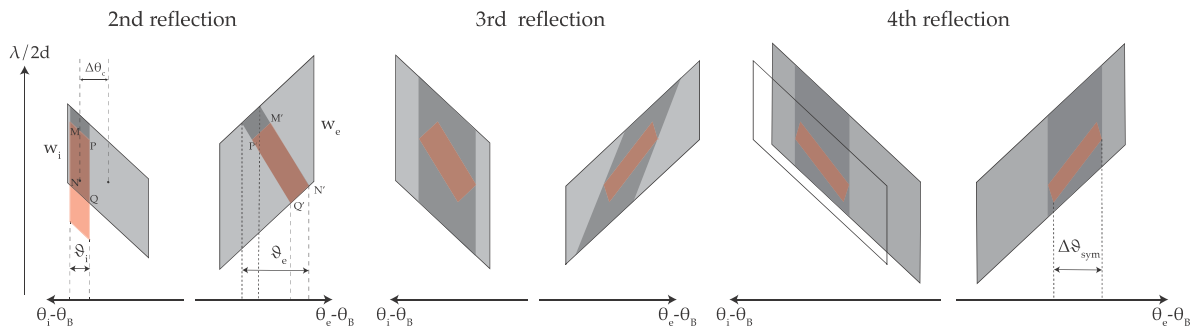


**FIGURE 4.** DuMond diagram for the subsequent reflections of the delay-adjustable branch for crystals arranged in the symmetric geometry.  $\vartheta_i$  and  $\vartheta_e$  are the incident and exit beam divergence from the 1st asymmetric reflection (2nd reflection) and  $\Delta\vartheta_{\text{sym}}$  is the energy dispersion after 4 bounces.

When the incidence beam bandwidth is comparable or larger than the energy acceptance of the channel-cuts, we analyze the impact of dispersion on the properties of the exit beam. This is illustrated by using DuMond diagram as shown in Fig. 4, where the light gray shaded paragon represents the acceptance window of each crystal reflection in the wavelength-angle phase-space within which the reflectivity is close to unity. The pink shaded areas represent the X-ray beam propagation through the subsequent reflections. The heights of the light gray paragon for the incident/exit

beam are determined by the Darwin width and the asymmetry factor  $b$ :

$$w_i = w_e/b = \frac{\Delta\lambda}{2d} = \frac{\Delta\lambda}{\lambda} \sin\theta_B = \frac{\Delta\theta_d}{\sqrt{b}} \cos\theta_B. \quad (6)$$

Dark gray areas illustrate the elastic scattering requirement and guide the energy-angle mapping from the entrance side to the dark gray area on the exit side. Assuming the incoming beam has a bandwidth that is much larger than the first Si(220) symmetric reflection, and a divergence of  $\vartheta_i \sim 2\mu\text{rad}$  (which is typical for hard X-ray FELs such as LCLS and SACLA), we use the first pink paragon to illustrate the beam entering the second reflection. From the DuMond diagram, we can extract that for a bandwidth of  $w_i$  (dark gray area), the dispersion incurred from an asymmetric reflection can be expressed as:

$$\vartheta_e - \vartheta_i = \frac{|w_e - w_i|}{\cos\theta_B} = \frac{1}{\sqrt{b}}|b - 1|\Delta\theta_d.$$

Note that due to the center shift  $\Delta\theta_c$  of the rocking curve of the second reflection which is asymmetric, only a fraction of the bandwidth  $\text{MN} = \Delta\theta_c \cos\theta_B$  is reflected by the second surface.

While continuing using DuMond diagrams for the subsequent two reflections, we can see that the 2nd asymmetric reflection (3rd reflection) has a larger acceptance angle and reflects the entire bandwidth, while reducing the beam divergence for each wavelength. However, the dispersive configuration between the 2nd and the 3rd reflection leads to additional dispersion, or increased ‘tilting’ of the pink region on the exit side. The 4th reflection, which is a symmetric reflection, preserves the bandwidth as well as the dispersion. For our geometry, the total dispersion of the output beam can be derived as:

$$\frac{\Delta\vartheta_{\text{sym}}}{\Delta w} = \frac{2(b - 1)}{b \cos\theta_B}.$$

For X-ray photon energy of 9 keV,  $\Delta w = \text{MN} \approx 1.17 \times 10^{-5}$ , an incident broadband parallel beam will incur  $9 \mu\text{rad}$  of angular spread over its band pass of 0.3 eV. On the other hand, we can arrange the crystals in an asymmetric

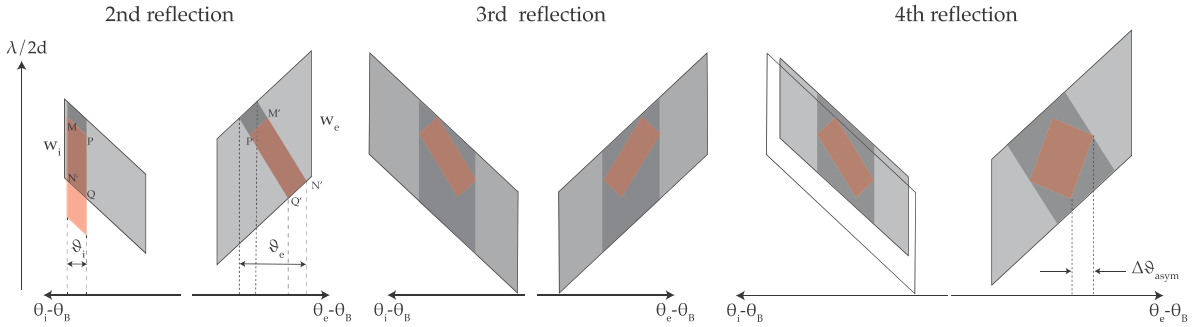


**FIGURE 5.** DuMond diagram for the subsequent reflections of the delay-adjustable branch for crystals arranged in the asymmetric geometry.  $\vartheta_i$  and  $\vartheta_e$  are the incident and exit beam divergence from the 1st asymmetric reflection (2nd reflection) and  $\Delta\vartheta_{\text{asym}}$  is the energy dispersion after 4 bounces.

configuration, as shown in Fig. 6(c), and its DuMond diagrams are presented in Fig. 5. Following the same derivation method as previously, the total dispersion of the output beam is:

$$\frac{\Delta\vartheta_{\text{asym}}}{\Delta w} = \frac{(b - 1)^2}{\cos\theta_B}$$

and is on the order of  $4 \mu\text{rad}$  for a 9 keV beam.

To summarize, when considering a broadband incoming X-ray beam, for the proposed system, the overall band pass will be narrower than a single symmetric Si(220) reflection, and the dispersion introduced by the asymmetric reflections can lead to a chromatic focus. In order to reduce that effect, an asymmetric configuration where we flip VCC2 is therefore preferred.

## Alternative Geometries and Configurations

In addition to the two configurations discussed previously, other combinations of the two variable-gap channel-cuts can realize a similar time-delay functionality. However, depending on the exact order of the symmetric and asymmetric reflections, the pulse front tilt and the dispersion effects will differ. 4 alternative configurations are shown in Fig. 6. Configuration (a) and (b) are both symmetric. In (a), we reversed the symmetric-asymmetric order within each channel-cut compared to the original concept as in Fig. 1. In (b), we reversed the asymmetry of both VCCs. In both cases, the resulting output beam will have the same size and divergence as the input beam. The overall bandwidth is also expected to be the same. On the other hand, the asymmetric configurations as shown in (c) will lead to a smaller output beam size in the scattering plane by a factor of  $b^2$ , albeit a reduced amount of pulse front tilt due to the partial cancellation of the tilting. Configuration (d) also reduces the pulse front tilt, with the output beam enlarged and further collimated.

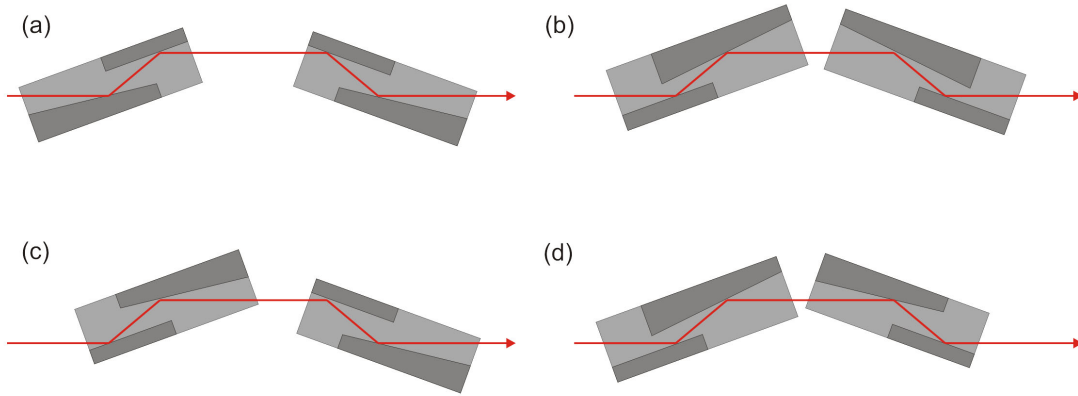


**FIGURE 6.** Examples of 4 different alternative geometric configurations of VCCSD's delay-adjustable branch.

Note that for the configurations discussed here, we have assumed identical miscut angles for the asymmetric-reflection surfaces in the two crystals for simplicity. By setting the asymmetry angles differently, there can be combinations where pulse front tilt and dispersion impact are minimized simultaneously or enhanced for specific applications. More detailed discussion of the impact of dispersion is beyond the scope of the current manuscript.

## CONCLUSION

We proposed a compact split-delay consisting of 4 channel-cuts. This X-ray optical arrangement can cover a photon energy range from 7 to 12 keV, and a delay time window on the order of 10s of picoseconds. It offers high stability, as the result of reflection pairs from monolithic channel-cuts and is therefore ideal tools for XPCS/XSVS experiments where the stability and control of the spatial overlap of the two beams is critical. It will also offer the possibility to do fast fly-delay-scan over the whole delay range. The tilted pulse front of the beam can be also be utilized for X-ray streaking applications for single-shot time domain measurements, such as performing pulse-to-pulse interferometric measurements of the beam coherence. Its picosecond delay timescale also opens new opportunities for single shot X-ray Pump X-ray Probe measurements using crossing-beam geometries, especially for high energy density science studies as well as X-ray wave mixing experiments.

## ACKNOWLEDGMENTS

We thank Alfred Baron, Paul Fuoss, Jerry Hastings, Ichiro Inoue, Taito Osaka, David Reis, Mark Sutton, Kenji Tamasaku, Makina Yabashi, for stimulating and helpful discussions. Use of the Linac Coherent Light Source (LCLS),

## REFERENCES

- [1] E. Allaria, D. Castronovo, P. Cinquegrana, P. Craievich, M. Dal Forno, M. Danailov, G. D’Auria, A. Demidovich, G. De Ninno, S. Di Mitri, *et al.*, [Nature Photonics](#) **7**, p. 913 (2013).
- [2] P. Emma *et al.*, [Nature](#) **4**, 641–647 (2010).
- [3] T. Ishikawa *et al.*, [Nature Photonics](#) **6**, p. 540544 (2012).
- [4] W. Ackermann, G. Asova, V. Ayvazyan, A. Azima, N. Baboi, J. Bähr, V. Balandin, B. Beutner, A. Brandt, A. Bolzmann, *et al.*, [Nature photonics](#) **1**, p. 336 (2007).
- [5] H.-S. Kang, C.-K. Min, H. Heo, C. Kim, H. Yang, G. Kim, I. Nam, S. Y. Baek, H.-J. Choi, G. Mun, *et al.*, [Nature Photonics](#) **11**, p. 708 (2017).
- [6] C. Bostedt, S. Boutet, D. M. Fritz, Z. Huang, H. J. Lee, H. T. Lemke, A. Robert, W. F. Schlotter, J. J. Turner, and G. J. Williams, [Rev. Mod. Phys.](#) **88**, p. 015007 (2016).
- [7] F. Decker, R. Akre, A. Brachmann, Y. Ding, D. Dowell, P. Emma, A. Fisher, J. Frisch, S. Gilevich, P. Hering, *et al.*, Proceedings of the 2010 Free Electron Laser Conference p. 467 (2010).
- [8] A. Marinelli, D. Ratner, A. Lutman, J. Turner, J. Welch, F.-J. Decker, H. Loos, C. Behrens, S. Gilevich, A. Miahnahri, *et al.*, [Nature communications](#) **6**, p. 6369 (2015).
- [9] A. A. Lutman, T. J. Maxwell, J. P. MacArthur, M. W. Guetg, N. Berrah, R. N. Coffee, Y. Ding, Z. Huang, A. Marinelli, S. Moeller, *et al.*, [Nature Photonics](#) **10**, p. 475 (2016).
- [10] C. Gutt, L.-M. Stadler, A. Duri, T. Autenrieth, O. Leupold, Y. Chushkin, and G. Grübel, [Optics express](#) **17**, 55–61 (2009).
- [11] I. Inoue, Y. Inubushi, T. Sato, K. Tono, T. Katayama, T. Kameshima, K. Ogawa, T. Togashi, S. Owada, Y. Amemiya, *et al.*, [Proceedings of the National Academy of Sciences](#) **113**, p. 1492 (2016).
- [12] K. R. Ferguson, M. Bucher, T. Gorkhover, S. Boutet, H. Fukuzawa, J. E. Koglin, Y. Kumagai, A. Lutman, A. Marinelli, M. Messerschmidt, *et al.*, [Science advances](#) **2**, p. e1500837 (2016).
- [13] W. Roseker, H. Franz, H. Schulte-Schrepping, A. Ehnes, O. Leupold, F. Zontone, A. Robert, and G. Grübel, [Optics letters](#) **34**, 1768–1770 (2009).
- [14] T. Osaka, T. Hirano, Y. Sano, Y. Inubushi, S. Matsuyama, K. Tono, T. Ishikawa, K. Yamauchi, and M. Yabashi, [Optics express](#) **24**, 9187–9201 (2016).
- [15] D. Zhu, Y. Sun, D. W. Schafer, H. Shi, J. H. James, K. L. Gumerlock, T. O. Osier, R. Whitney, L. Zhang, J. Nicolas, *et al.*, [Proceedings of SPIE](#) **10237**, p. 102370R (2017).
- [16] R. Alonso-Mori, C. Caronna, M. Chollet, R. Curtis, D. S. Damiani, J. Defever, Y. Feng, D. L. Flath, J. M. Glownia, S. Lee, *et al.*, [Journal of synchrotron radiation](#) **22**, 508–513 (2015).
- [17] M. Chollet, R. Alonso-Mori, M. Cammarata, D. Damiani, J. Defever, J. T. Delor, Y. Feng, J. M. Glownia, J. B. Langton, S. Nelson, *et al.*, [Journal of synchrotron radiation](#) **22**, 503–507 (2015).
- [18] U. Bonse and M. Hart, [Applied Physics Letters](#) **6**, 155–156 (1965).
- [19] J. Als-Nielsen and D. McMorrow, *Elements of modern X-ray physics* (John Wiley & Sons, 2011).
- [20] S. Brauer, G. Stephenson, and M. Sutton, [Journal of synchrotron radiation](#) **2**, 163–173 (1995).
- [21] B. W. Batterman and H. Cole, [Reviews of modern physics](#) **36**, p. 681 (1964).
- [22] T. Osaka, T. Hirano, M. Yabashi, Y. Sano, K. Tono, Y. Inubushi, T. Sato, K. Ogawa, S. Matsuyama, T. Ishikawa, *et al.*, [Proceedings of SPIE](#) **9210**, p. 921009 (2014).
- [23] C. David, P. Karvinen, M. Sikorski, S. Song, I. Vartiainen, C. Milne, A. Mozzanica, Y. Kayser, A. Diaz, I. Mohacsi, *et al.*, [Scientific reports](#) **5** (2015).
- [24] M. Buzzi, M. Makita, L. Howald, A. Kleibert, B. Vodungbo, P. Maldonado, J. Raabe, N. Jaouen, H. Redlin, K. Tiedtke, P. M. Oppeneer, C. David, F. Nolting, and J. Lüning, [Scientific reports](#) **7**, p. 7253 (2017).
- [25] J. Amann, W. Berg, V. Blank, F.-J. Decker, Y. Ding, P. Emma, Y. Feng, J. Frisch, D. Fritz, J. Hastings, *et al.*, [Nature photonics](#) **6**, 693–698 (2012).